RSC Advances

PAPER

View Article Online
View Journal | View Issue

Cite this: *RSC Adv.*, 2025, **15**, 22154

Improving the luminescence properties of the near-infrared phosphor $Ca_{0.8}Sr_{0.2}O:Eu^{2+}$ *via* energy transfer and its application in the concentration detection of ethanol solutions†

Yuxuan Liang,[a] Pengfei Du,[b] Yanhong Wei,[c] Xurui Hu,*[b] Xiaojie Li,[a] Zhijun Wang,[a] Jie Gong,[a] Mengdi Liu,[a] Panlai Li[a] and Wenge Ding*[a]

Received 8th April 2025
Accepted 4th June 2025

DOI: 10.1039/d5ra02418h

rsc.li/rsc-advances

In this work, a near-infrared (NIR) phosphor $Ca_{0.8}Sr_{0.2}O:Eu^{2+}$ was prepared *via* a solid-state method, and its luminescence properties were improved by co-doping with Ce^{3+} ions. The decay curves of $Ca_{0.8}Sr_{0.2}O:Ce^{3+}$, Eu^{2+} confirmed that there was an obvious energy transfer from Ce^{3+} to Eu^{2+}, which enhanced the quantum efficiency of $Ca_{0.8}Sr_{0.2}O:Eu^{2+}$. The thermal stability can also be enhanced by introducing Ce, which reduces the probability of non-radiative transitions at elevated temperatures, thereby minimizing electron loss. An NIR light emitting diode (LED) was fabricated by combining a blue LED chip with $Ca_{0.8}Sr_{0.2}O:Ce^{3+}$, Eu^{2+}, which was applied for the concentration detection of ethanol solutions.

1. Introduction

In recent years, near-infrared (NIR) light has found widespread application in fields such as night vision, biological tissue penetration, solution detection, food quality detection, and plant growth. This is because NIR light possesses several advantageous properties: it has strong penetration capability, causes minimal damage to the human body, is invisible to the human eye, and overlaps with certain organic functional groups like C–H (2980 cm^{-1}) and C–O (1100 cm^{-1}).[1–9] As the core component for these applications, the NIR light source needs to meet the conditions of broadband emission, good stability, miniaturization and fast response.[10] Traditional NIR light sources (such as the halogen tungsten lamp) can emit wide-range NIR light; however, they have the disadvantages of high energy consumption, large volume and short life, which cannot meet the requirements for practical use.[11,12] NIR LED is another NIR light source, which is made up of a combination of multiple NIR LEDs of different wavelengths arranged in an array to meet the demand of a broadband NIR light source. Although this NIR light source exhibits a long life and high efficiency, its large volume and the emission of various spectra by different LEDs consistently affect the overall spectral type of the light source with changes in temperature and time. These deficiencies make NIR LEDs unable to meet practical requirements. Currently, NIR phosphor conversion LEDs are considered ideal NIR light sources to satisfy the practical demands of the above-mentioned fields owing to their small size, long life and fast response.[13–15] The main preparation method of an NIR pc-LED involves coating the broadband NIR phosphor onto a mature blue LED; hence, it is crucial to explore efficient broadband NIR phosphors.

Currently, NIR phosphors can be obtained by doping with the following ions: trivalent rare-earth ions (Pr^{3+}, Yb^{3+}, Nd^{3+}), transition metal ions (Mn^{4+}, Ni^{2+}, Cr^{3+}), and divalent rare-earth ions (Eu^{2+}). Because electronic transitions inside the f–f electronic configuration of trivalent rare earth ions is forbidden and has a weak absorption capacity, such materials exhibit low luminous efficiency and a narrow emission bandwidth, which cannot meet the requirements of efficient wide-band NIR light sources, limiting their applications. Mn^{4+} ions tend to occupy a strong crystal field environment. They usually exhibit narrow band emissions, and the spectrum is not easy to regulate, thus lacking the requirements for a broadband emission NIR light source. Although the emission wavelength of Ni^{2+} ions is greater than 1000 nm, their luminescence efficiency is low with a relatively poor thermal stability, and it cannot be effectively applied as an NIR light source. Cr^{3+} exhibits a broadband NIR emission at $^4T_2 \rightarrow {}^4A_2$ level transition. This transition is outside the 3d electron layer, and hence, it is vulnerable to the influence of

[a]National-Local Joint Engineering Laboratory of New Energy Photoelectric Devices, Hebei Key Laboratory of Optic-electronic Information and Materials, College of Physics Science & Technology, Hebei University, Baoding 071002, China. E-mail: dwg@hbu.edu.cn

[b]School of Physical Science and Technology, Ningbo University, Ningbo 315211, China. E-mail: huxurui@nbu.edu.cn

[c]Working Committee for the Care of the Next Generation, Hebei University, Baoding 071002, China

† Electronic supplementary information (ESI) available. See DOI: https://doi.org/10.1039/d5ra02418h

intensity changes in the crystal field. Consequently, Cr^{3+} will produce different luminescence under different conditions of crystal field strength. However, the Cr^{3+}-doped NIR phosphors will inevitably contain toxic and harmful Cr^{6+}, which greatly limits their application in food safety testing and human body monitoring. The luminescence of Eu^{2+} (a rare earth ion) originates from its 5d → 4f transition, and because of the naked leakage of the 5d level on the electron layer surface, Eu^{2+} is also susceptible to the crystal field environment, indicating that the luminescence of Eu^{2+} can be easily regulated. Therefore, Eu^{2+}-doped NIR phosphors have become a research hotspot in the field of NIR phosphors. In this work, a broadband NIR phosphor $Ca_{0.8}Sr_{0.2}O:Eu^{2+}$ was prepared. It was observed that the energy transfer between Ce^{3+}–Eu^{2+} was realized, quantum efficiency of $Ca_{0.8}S_{r0.2}O:Eu^{2+}$ was improved from 36.7% to 45.8%, and the thermal stability was improved from 27.4% to 40.8%. The prepared NIR pc-LEDs were explored for the concentration detection of ethanol solutions. The results demonstrate that this study offers a novel approach for developing NIR phosphors.

2. Experimental

2.1. Synthesis

Two phosphors, namely, $Ca_{0.8}Sr_{0.2-x}O:xCe^{3+}$ and $Ca_{0.8-y}Sr_{0.2}O:0.4\%\ Ce^{3+}, yEu^{2+}$ were prepared *via* a high-temperature solid-state method. High-purity (99.99%, Aladdin) $CaCO_3$, $SrCO_3$, Eu_2O_3, and CeO_2 were used as raw materials, and they were precisely weighed in accordance with their stoichiometric ratios. The weighed samples were then placed in a clean agate mortar and ground thoroughly for 20–30 minutes. The ground powder was then transferred to either a corundum or graphite crucible and was placed in a tube furnace for high-temperature sintering. The temperature of the sintered samples was first raised from room temperature to 500 °C at 5 °C min^{-1} for 30 minutes, then increased to 900 °C for 80 minutes, and finally elevated to 1200 °C for 60 minutes. The samples were allowed to cool to room temperature. Subsequently, they were ground again to form a homogeneous and fine powder for characterization and testing.

2.2. NIR pc-LED fabrication

Phosphor-converted LED (pc-LED): First, the phosphor powder, B glue, and A glue were weighed in a 5 : 4 : 1 ratio. Then, the weighed powder and glues were placed in a beaker for 40 minutes to ensure thorough mixing. Finally, the mixture was coated onto an LED chip with a suitable excitation wavelength and dried in an oven that was pre-set at 353 K for 2 hours to bond it to the chip.

2.3. Characterizations

The instrument used for the measurements was a Bruker AXS's D8 Advance X-ray diffractometer (Germany) with a Cu-Kα radiation source. The scan range was 10° to 80° (2θ), operating at a precision of 0.0001°, with an applied voltage of 40 kV and a current of 40 mA. The structure was further optimized using the general structure analysis system (GSAS-II). Ultrahigh-resolution surface micrographs of the nanoscale materials were acquired using an FEI Nova NanoSEM 450 scanning electron microscope, which also enabled the analysis of surface elemental composition (type and quantity). Surface analysis of the sample was conducted using an ESCALAB 250Xi X-ray photoelectron spectrometer, providing detailed information on the elemental composition, chemical states, molecular structures, and chemical bonding configurations of the phosphors. The analysis chamber operated at an ultimate vacuum of 5×10^{-1} mbar, with an energy scan range of 0 to 5000 eV and an energy resolution of 0.45 eV. The system featured independent analysis and injection chambers. A U4100 spectrometer with a wavelength range of 240 to 17 000 nm, a standard four-hole integrating sphere (with an opening rate of less than 7.8%), and a diameter of 60 mm was utilized, and it could accommodate a maximum sample size of 200 × 200 mm. Barium sulfate ($BaSO_4$) was used as the reference for transmission and absorption characterizations. Steady-state fluorescence emission spectra, excitation spectra, variable temperature spectra, and quantum efficiency were determined using a Fluorolog-3 fluorescence spectrometer (HORIBA Instruments, Inc.). The excitation source was a 450 W Xenon lamp, with a scanning speed of 1200 nm min^{-1} and an integration time of 0.1s.

3. Results and discussion

3.1. Phase information

Fig. 1(a) illustrates the layered arrangement of the CaO crystal structure. Fig. S1† and 1(b) show the XRD patterns of $Ca_{0.8}Sr_{0.2-x}O:xCe^{3+}$ ($x = 0.1$–1.3%) and yEu^{2+} ($y = 0\%$, 0.1%), and it can be seen that the synthesized samples matched with the CaO standard phase (PDF #001-1160) in the inorganic crystal structure database, indicating that the synthesized samples possessed a single phase. As we synthesized a sample with Sr^{2+}, partially replacing Ca^{2+}, the XRD pattern exhibited a tendency to be shifted in the direction of a small angle compared with the Standardized card. GSAS2 refinement software was employed to further investigate the effect of Ce^{3+}–Eu^{2+} on the crystal structure of CSO. This refinement also aimed at determining whether the position of Eu^{2+} was changed. As exhibited in Fig. 1(c), for CSO:0.4% Ce^{3+} and CSO:0.4% Ce^{3+}, 0.1% Eu^{2+}, the profile factors R_p, R_{wp}, and χ^2 met the refinement requirements. This indicates that the crystal cell parameters obtained through refinement are reasonable, and this applies to other doping concentrations as well as $Ca_{0.8-x}Sr_{0.2}O:0.4\%\ Ce^{3+}, yEu^{2+}$ ($y = 0$–0.12%). The crystal cell parameters obtained *via* refinement are depicted in Table 1. As depicted in Fig. 1(d), the lattice parameters $a/b/c$ and volume V increase with the Eu^{2+} concentration. This indicates that Eu^{2+} ions still occupy the Ca^{2+} sites without changing their positions. Fig. 1(e) depicts the XPS spectra of CSO:0.4% Ce^{3+}, 0.1% Eu^{2+}; the binding energies corresponding to Ca-2p, Sr-3d, and O-1s can be well observed in the whole spectra. Owing to the small doping contents of Ce and Eu, they could only be observed in the fine spectrum, as depicted in the inset of Fig. 1(e). Additionally, the Eu-$3d_{5/2}$ and the Ce^{3+} corresponding Ce-$3d_{5/2}$ energy combinations were also observed. Fig. 1(f) presents the SEM image and elemental mapping of CSO:0.4% Ce^{3+}, 0.1% Eu^{2+}. The synthesized

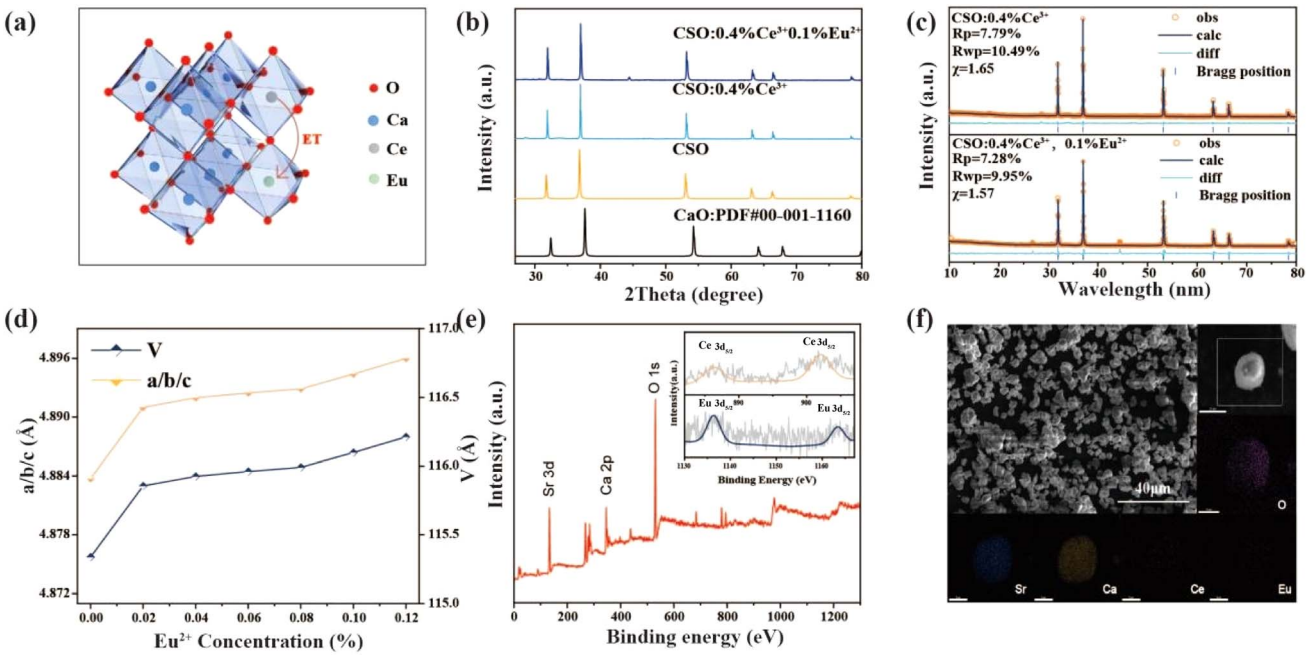

Fig. 1 (a) Crystal structure of CaO; (b) XRD patterns of $Ca_{0.8}Sr_{0.2}O$, $Ca_{0.8}Sr_{0.196}O$(CSO):0.4% Ce^{3+} and CSO:0.4% Ce^{3+}, 0.1% Eu^{2+}; (c) rietveld refinement of CSO:0.4% $Ce^{3+}$and CSO:0.4% Ce^{3+}, 0.1% Eu^{2+}; (d) lattice parameters *a*/*b*/*c* and *V* with Eu^{2+} concentration; (e) XPS full survey spectrum of CSO:0.4% Ce^{3+}, 0.1% Eu^{2+}, inset: high-resolution XPS of Ce^{3+} and Eu^{2+}; and (f) SEM and element mapping images of CSO:0.4% Ce^{3+}, 0.1% Eu^{2+}.

Table 1 Crystal cell parameters for $Ca_{0.8}Sr_{0.2}O$:0.4% Ce^{3+}, yEu^{2+} (y = 0–0.12%) obtained *via* refinement

$y(Eu^{2+})$	Cell parameters (Å^3)	Cell volume (Å^3)	R_{wp} (%), R_p (%), χ^2
0%	$a/b/c = 4.87572$	115.909	12.38, 8.5, 1.97
0.02%	$a/b/c = 4.88299$	116.428	14.59, 10.13, 2.08
0.04%	$a/b/c = 4.88396$	116.498	13.84, 9.8, 1.97
0.06%	$a/b/c = 4.88446$	116.533	12.56, 9.23, 1.76
0.08%	$a/b/c = 4.88488$	116.563	9.39, 6.79, 1.59
0.1%	$a/b/c = 4.88638$	116.671	9.95, 7.28, 1.57
0.12%	$a/b/c = 4.88797$	116.785	10.99, 9.8, 1.55

samples exhibited fairly uniform particle sizes of approximately 10 μm. Five elements, namely, Ca, Sr, O, Eu, and Ce were successfully identified.

3.2. Luminescence properties

Fig. 2(a) presents the emission spectrum of CSO:Ce^{3+} and the excitation spectrum of CSO:Eu^{2+}. The spectral overlap between 500 nm and 700 nm suggested the potential energy transfer from Ce^{3+} to Eu^{2+}. In order to further improve the CSO:Ce^{3+} performance by identifying the optimal Ce^{3+} concentration, the emission spectra of CSO:$x$$Ce^{3+}$ (x = 0.1–1.3%) were investigated under a 467 nm excitation, and the optimal Ce^{3+} concentration was obtained as x = 0.4% Fig. 2(b). Fig. 2(c) shows the emission spectra of CSO:0.4% Ce^{3+}, yEu^{2+} (y = 0–0.12%) under an excitation of 467 nm, and the NIR emission peak belonging to Eu^{2+} appeared at y = 0.06%. Owing to concentration quenching, the NIR emission intensities first increased and then decreased as the Eu^{2+} concentration gradually increased, and the maximum value appeared at y = 0.1%. Fig. 2(d) presents the decay curves of CSO:0.4% Ce^{3+}, yEu^{2+} (y = 0–0.12%) at 581 nm, demonstrating the occurrence of energy transfer between Ce^{3+}–Eu^{2+}, and all the decay curves could be well fitted using the biexponential function as follows:[16–18]

$$I(t) = I_0 + A_1 \exp\left(-\frac{t}{\tau_1}\right) + A_2 \exp\left(-\frac{t}{\tau_2}\right) \quad (1)$$

where $I(t)$ is the luminescence intensity, A_1 and A_2 are constants, τ is the average lifetime, and τ_1 and τ_2 are the fast decay and slow decay lifetimes, respectively. The average lifetime τ can be obtained using the following formula:[19,20]

$$\tau = (A_1\tau_1^2 + A_2\tau_2^2)/(A_1\tau_1 + A_2\tau_2) \quad (2)$$

The calculations showed that the average lifetimes of Ce^{3+} ions were 33.48 ns, 28.46 ns, 20.53 ns, 13.73 ns, 10.59 ns, 5.01 ns and 4.68 ns for y = 0%, 0.02%, 0.04%, 0.06%, 0.08%, 0.10%, and 0.12%, respectively. Clearly, the emission peak attributed to Ce^{3+} decreased monotonically with increasing Eu^{2+} concentration, proving the occurrence of energy transfer between Ce^{3+}–Eu^{2+}. Energy transfer efficiency is an important parameter, which can be calculated by the decrease in emission intensity using the following formula:[21]

$$\eta_T = 1 - I_s/I_{s0} \quad (3)$$

where I_{s0} and I_s represent the luminescence intensity of Ce^{3+} ions without and with Eu^{2+} ions, respectively, and η_T is the value

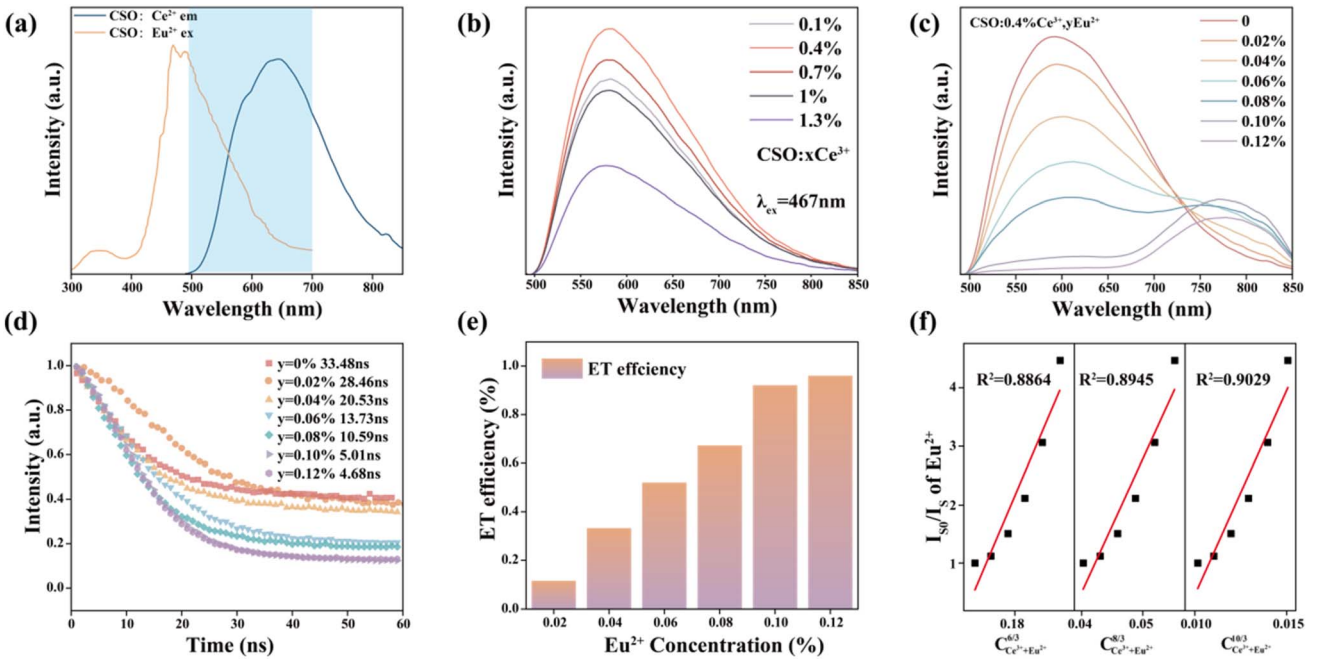

Fig. 2 (a) Emission spectrum of CSO:Ce^{3+} and excitation spectrum of CSO:Eu^{2+}; (b) emission spectra of CSO:Ce^{3+} ($x = 0.1$–1.3%); (c) emission spectra of CSO:0.4% Ce^{3+}, yEu^{2+} ($y = 0$–0.12%); (d) decay curves of CSO:0.4% Ce^{3+}, yEu^{2+} ($y = 0$–0.12%); (e) energy transfer efficiency of CSO:0.4% Ce^{3+}, yEu^{2+} ($y = 0$–0.12%) ($\lambda_{ex} = 467$ nm); and (f) dependence of (I_{s0}/I_s) of Ce^{3+} on $C^{6/3}_{Ce+Eu}$, $C^{8/3}_{Ce+Eu}$ and $C^{10/3}_{Ce+Eu}$.

of energy transfer efficiency. The calculated results are depicted in Fig. 2(e). The energy transfer efficiency reached a maximum of 96.6% at $x = 0.12$%.

A concentration quenching phenomenon can arise from either electric multipolar interactions or exchange interactions. When the critical distance exceeds 0.5 nm, the electric multipolar interactions are likely to induce concentration quenching; conversely, at shorter distances, the exchange interactions tend to dominate.[22] As reported by Blaszse, the critical transfer distance (R_c) can be expressed as:[23]

$$R_c = 2[3V/4\pi X_c N]^{1/3} \quad (4)$$

where N represents the number of host cations in the unit cell, V represents the volume per unit cell, and X_c represents the total critical concentration of Ce^{3+} and Eu^{2+} ions. For CSO substrate, $V = 0.115909$ nm^3, $N = 14$, $X_c = 0.005$; therefore, R_c is approximately 1.468 nm, which is significantly larger than 0.5 nm, indicating that the electric multipolar interaction caused a nonradiative concentration quenching of Ce^{3+}–Eu^{2+} ions. For electrical multipolar interactions, it may include the dipole–dipole (d–d), the dipole–quadrupole (d–q), and the quadrupole–quadrupole (q–q) interactions.[24] According to Dexter's energy transfer theory, the multipolar interaction[24,25] can be expressed using the linear relationship in the following formula:

$$\frac{\eta_0}{\eta_S} \propto C^{n/3}_{S+A} \quad (5)$$

where η_0 and η_S are the energy transfer efficiency of Ce^{3+} ions in the samples without and with Eu^{2+} ions, respectively. The relative luminescence intensity ratio (I_s/I_{s0}) can approximately replace the ratio of η_0/η_S. C_{S+A} is the total concentration of Ce^{3+} and Eu^{2+} ions in the sample, and $n = 6$, 8, or 10, indicating a d–d interaction, d–q interaction or q–q interaction, respectively. Fig. 2(f) depicts the linear relationship between I_s/I_{s0} and $C^{n/4}_{S+A}$. An optimal linear behavior was obtained at $n = 10$, indicating that q–q interactions determined the mechanism of energy transfer between Ce^{3+} and Eu^{2+} ions.

Fig. 3(a) displays the thermal spectra of CSO:0.4% Ce^{3+}, 0.1% Eu^{2+}. The emission intensity reached 40.8% (398 K) of that at room temperature (298 K), which is 13.4% higher than that of CSO:0.4% Ce^{3+}. To explore why thermal stability increased, Fig. 3(b) demonstrates the pyrothermal spectra of two samples before and after Ce^{3+} doping. Obviously, the pyrothermal curve intensity for the sample doped only with Eu^{2+} is nearly zero, indicating no trap. Conversely, after introducing isovalent Ce^{3+}, a peak appears in the pyroheat curve around 343 K. This suggests that blending Ce^{3+}–Eu^{2+} has created a shallow trap. The reason for occurrence of the trap was that the introduction of Ce^{3+} destroyed the original charge balance of the matrix. In order to maintain the charge balance, two Ce^{3+} replaced three Sr^{2+} to creating one doubly negatively charged Sr vacancy (V''_{Sr}) and two positively charged defects $[Ce^{3+}]^{\cdot}_{Sr}$. The substitution process was as follows.

$$3Sr^{2+} + 2Ce^{3+} \rightarrow V''_{Sr} + 2[Ce^{3+}]^{\cdot}_{Sr} \quad (6)$$

The schematic of Ce^{3+}–Eu^{2+} energy transfer and thermal stability enhancement is given in Fig. 3(c). The electrons of Ce^{3+} jumped from the 4f ground state to 5d energy level after getting excited by a 467 nm light. A part of the electrons returned to the 4f ground state *via* radiative leaps and produced a broadband

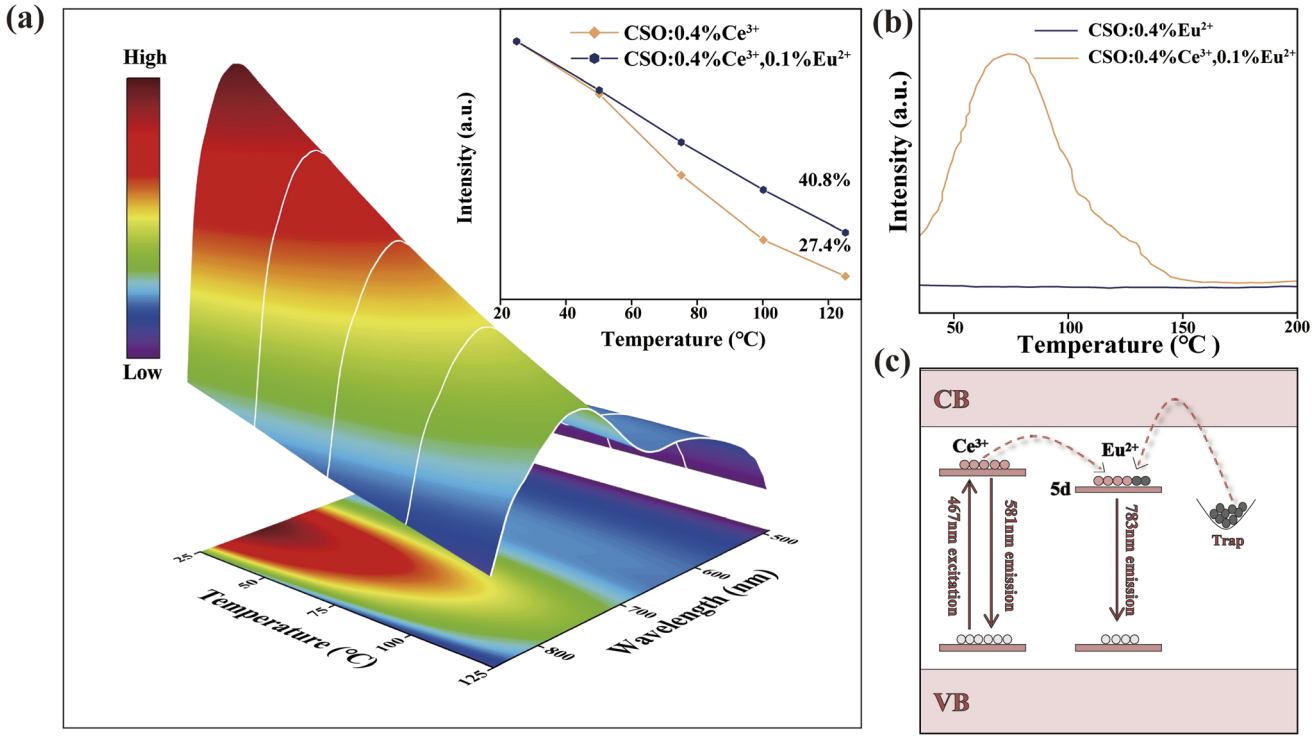

Fig. 3 (a) Temperature-dependent PL spectra of CSO:0.4% Ce^{3+},0.1% Eu^{2+}, inset: intensities of CSO:0.4% Ce^{3+} and CSO:0.4% Ce^{3+}, 0.1% Eu^{2+} at different temperatures; (b) TL curves of CSO:0.1% Eu^{2+} and CSO:0.4% Ce^{3+}, 0.1% Eu^{2+}; and (c) mechanism diagram showing Ce^{3+}–Eu^{2+} energy transfer and thermal stability enhancement.

yellow luminescence, and another part of the electrons got transferred to the 5d energy level of Eu^{2+} *via* energy transfer and returned to the 4f ground state *via* radiative leaps, producing a broadband NIR emission. In addition, a small fraction of electrons was trapped and stored therein. In luminescent materials, nonradiative transitions are mainly caused by factors such as lattice vibrations and defects. When the temperature increases, the lattice vibration intensifies, which makes it easier for the electrons to return from the excited state to the ground state, thus increasing the probability of non-radiative transitions. In addition, defects in the material can have a significant effect on the non-radiative transitions. The presence of defects disrupts the periodic potential field of the lattice, creating localized potential wells, in which the electrons undergo non-radiative leaps. In this study, we observed that when the temperature was increased, the electrons stored in the traps jumped out of the traps owing to thermal excitation and moved through the conduction band to the 5d energy level of Eu^{2+}. This process effectively replaced a part of the electron loss due to the increased probability of nonradiative leaps as a result of temperature elevation, resulting in an improvement in the thermal stability of the sample. In addition, we experimentally measured the quantum efficiency of the system to be 45.8% (as shown in Fig. S2†). This result also reflected that the material was thermally stable to a certain extent, and it can effectively suppress the effect of nonradiative transitions on the luminescence performance, demonstrating more intuitively the effects of lattice vibrations and defect changes on nonradiative transitions.

4. Application

Organic solutions contain a large number of chemical bonds such as C–H, C–O and O–H; these chemical bonds can absorb near infrared light of specific wavelengths, and accordingly, the concentration of the organic solvents can be detected using an NIR light. An NIR pc-LED was prepared by combining a blue LED with CSO:0.4% Ce^{3+}, 0.1% Eu^{2+} for concentration detection of ethanol (C_2H_5OH) solutions. Fig. 4(a) exhibits the experimental design for solution concentration detection. The NIR pc-LED emitted NIR light, which was passed through cuvettes with different concentrations of ethanol solution, and was finally received by the detector and presented on a computer in the form of a spectrum. Fig. 4(b) displays the experimental device. Fig. 4(c) exhibits the transmission spectra of the NIR pc-LED after passing through 0%, 20%, 40%, 60% and 80% ethanol solutions. It can be seen that as the concentration of the ethanol solution gradually increased, the absorption also gradually increased but the luminescence intensities gradually decreased. The intensity of the NIR light after passing through the ethanol solution and the concentration of the components in the sample complied with the Lambert–Beer law:

$$A = \log\frac{I_0}{I} = \varepsilon bc, \quad (7)$$

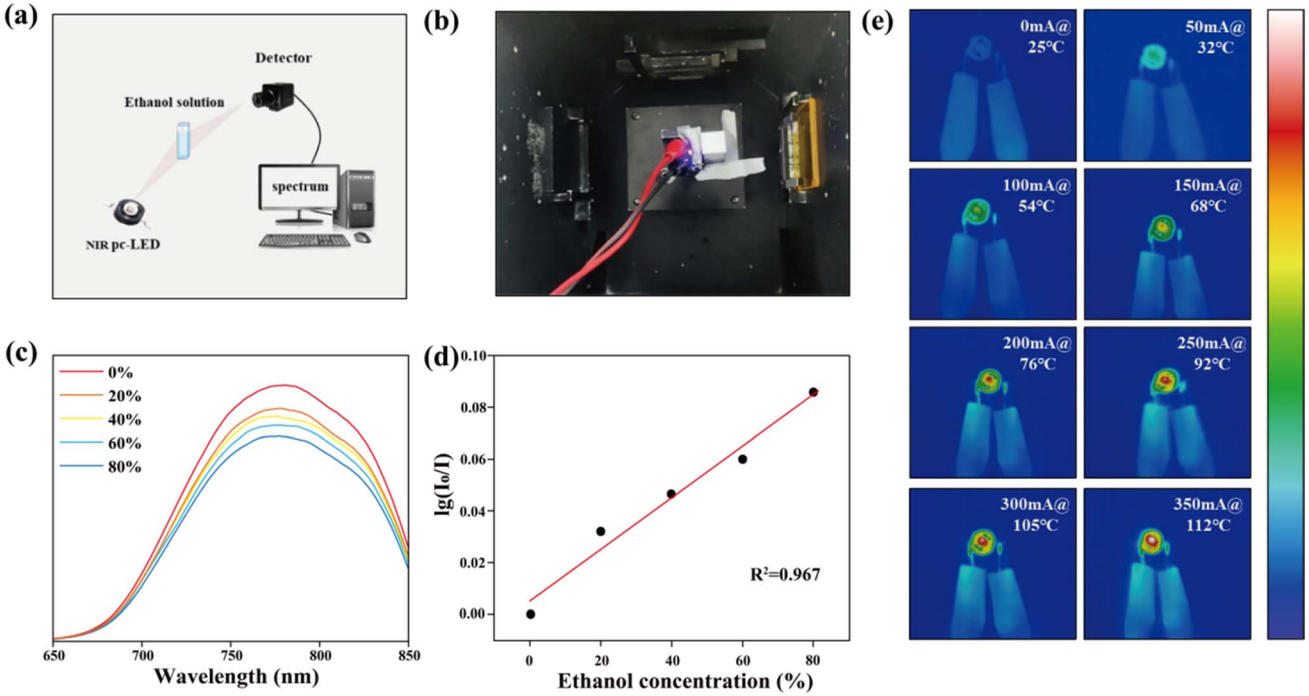

Fig. 4 (a) Schematic of the experimental design for solution concentration detection; (b) experimental device; (c) transmission spectra of the NIR pc-LED after passing through different concentrations of ethanol; (d) relationship between absorbance and concentration of ethanol solution; and (e) thermal images of the NIR pc-LED at different working currents ranging between 0–350 mA.

where A is the absorbance, I_0 is the initial intensity, I is the intensity after passing through different concentrations of ethanol solutions, ε denotes the molar absorptivity of the analyte, c is the concentration of the fraction to be tested, and b is the effective path length. The dependence of the luminescence intensity on the ethanol concentration was calculated. As illustrated in Fig. 4(d), the absorbance and ethanol concentration showed a good linear correlation after the fitting, and the fit reached $R^2 = 0.967$, indicating that the phosphor could offer a good application prospect in the field of concentration detection of solutions. The NIR pc-LED produced different amount of heat under different working currents, and thus, the temperature of the NIR pc-LED increased. Fig. 4(e) exhibits the pyrometer image of the NIR pc-LED under different working currents (0–350 mA). It can be seen that the temperature gradually increased with increasing working current, and when the working current reached 350 mA, the temperature reached 385 K.

5. Conclusions

In conclusion, the novel NIR phosphor $Ca_{0.8}Sr_{0.2}O:Eu^{2+}$ was synthesized *via* a solid-state method. When Ce^{3+} ions were introduced, the luminescence performance of $Ca_{0.8}Sr_{0.2}O:Ce^{3+}$, Eu^{2+} was obviously improved. Importantly, the quantum efficiency of $Ca_{0.8}Sr_{0.2}O$:0.1% Eu^{2+} increased from 36.7% to 45.8%, and the thermal stability at 398 K increased from 27.4% to 40.8%. The decay curves confirmed that the reason for this result was the occurrence of energy transfer between Ce^{3+}–Eu^{2+}. The NIR pc-LED prepared by combining $Ca_{0.8}Sr_{0.2}O$:0.4% Ce^{3+}, 0.1% Eu^{2+} with a blue LED chip verified its promising application in the concentration detection of organic solutions.

Data availability

All relevant data are within the manuscript and its ESI.†

Conflicts of interest

The authors declare that they have no conflicts of interest.

Acknowledgements

This work was supported by the National Natural Science Foundation of China (No. 51902080) and the Natural Science Foundation of Hebei Province, China (No. A2023201014).

References

1 L. Zhang, H. Xu and M. Gu, Use of signal to noise ratio and area change rate of spectra to evaluate the visible/NIR spectral system for fruit internal quality detection, *J. Food Eng.*, 2014, **139**, 19–23.
2 A. Guelpa, F. Marini, A. du Plessis, R. Slabbert and M. Manley, Verification of authenticity and fraud detection in South African honey using NIR spectroscopy, *Food Control*, 2017, **73**, 1388–1396.
3 K. Deng, R. Y. Zhang, L. Yuan, H. Wu and Y. Hu, Luminescent properties of broad band far red emitting

$Zn_3Ga_2GeO_8$:Mn^{2+}, Ca^{2+} phosphors for indoor plant growth LED, *Appl. Phys. A: Mater. Sci. Process.*, 2023, **129**(1), 69–75.

4 A. Dalle Zotte, M. Ottavian, A. Concollato, L. Serva, R. Martelli and G. Parisi, Authentication of raw and cooked freeze-dried rainbow trout (Oncorhynchus mykiss) by means of near infrared spectroscopy and data fusion, *Food Res. Int.*, 2014, **60**, 180–188.

5 Q. Zhang, D. Liu, P. Dang, H. Lian, G. Li and J. Lin, Two selective sites control of Cr^{3+}-doped ABO_4 phosphors for tuning ultra-broadband near-infrared photoluminescence and multi-applications, *Laser Photon. Rev.*, 2022, **16**(2), 2100459–2100464.

6 S. He, P. Li, Y. Ren, G. Wei, Y. Wang, Y. Yang, R. Li, J. Li, Y. Shi, X. Shi and Z. Wang, Near-infrared broadband $ZnTa_2O_6$:Cr^{3+} phosphor for pc-LEDs and its application to nondestructive testing, *Inorg. Chem.*, 2022, **61**(29), 11284–11292.

7 X. Zou, X. Wang, H. Zhang, Y. Kang, X. Yang, X. Zhang, M. S. Molokeev and B. Lei, A highly efficient and suitable spectral profile Cr^{3+}-doped garnet near-infrared emitting phosphor for regulating photomorphogenesis of plants, *Chem. Eng. J.*, 2022, **428**, 132003–132011.

8 Y. Shi, Z. Wang, J. Peng, Y. Wang, S. He, J. Li, R. Li, G. Wei, Y. Yang and P. Li, Achieving the ultra-broadband near-infrared $La_3SnGa_5O_{14}$:Cr^{3+}phosphor *via* multiple lattice sites occupation for biological nondestructive detection and night-vision technology, *Mater. Today Adv.*, 2022, **16**, 100305–100312.

9 N. Yeh and J. P. Chung, High-brightness LEDs-Energy efficient lighting sources and their potential in indoor plant cultivation, *Renewable Sustainable Energy Rev.*, 2009, **13**(8), 2175–2180.

10 L. Zhang, S. Zhang, Z. Hao, X. Zhang, G. H. Pan, Y. Luo, H. Wu and J. Zhang, A high efficiency broad-band near-infrared $Ca_2LuZr_2Al_3O_{12}$:Cr^{3+} garnet phosphor for blue LED chips, *J. Mater. Chem. C*, 2018, **6**(18), 4967–4976.

11 N. A. Mohd Aziz, N. Arsad, P. S. Menon, S. Shaari, Z. Md Yusof and A. R. Laili, An assessment study of absorption effect: LED vs tungsten halogen lamp for noninvasive glucose detection, *J. Innovative Opt. Health Sci.*, 2015, **8**(2), 1550013–1550017.

12 H. Zeng, T. Zhou, L. Wang and R. Xie, Two-site occupation for exploring ultra-broadband near-infrared phosphor-double-perovskite La_2MgZrO_6:Cr^{3+}, *Chem. Mater.*, 2019, **31**(14), 5245–5253.

13 M. Ye, Z. Gao, Z. Li, Y. Yuan and T. Yue, Rapid detection of volatile compounds in apple wines using FT-NIR spectroscopy, *Food Chem.*, 2016, **190**, 701–708.

14 S. Sarkar, P. Le, J. Geng, Y. Liu, Z. Han, M. U. Zahid, D. Nall, Y. Youn, P. R. Selvin and A. M. Smith, Short-wave infrared quantum dots with compact sizes as molecular probes for fluorescence microscopy, *J. Am. Chem. Soc.*, 2020, **142**(7), 3449–3462.

15 A. Zabiliūtė, S. Butkutė, A. Žukauskas, P. Vitta and A. Kareiva, Sol-gel synthesized far-red chromium-doped garnet phosphors for phosphor-conversion light-emitting diodes that meet the photomorphogenetic needs of plants, *Appl. Opt.*, 2014, **53**(5), 907–914.

16 X. Zhang, J. Xu, Z. Guo and M. Gong, Luminescence and energy transfer of dual-emitting solid solution phosphors $(Ca, Sr)_{10}Li(PO_4)_7$:Ce^{3+}, Mn^{2+} for ratiometric temperature sensing, *Ind. Eng. Chem. Res.*, 2017, **56**(4), 890–898.

17 M. Li, J. Zhang, J. Han, Z. Qiu, W. Zhou, L. Yu, Z. Li and S. Lian, Changing Ce^{3+} content and codoping Mn^{2+} induced tunable emission and energy transfer in $Ca_{2.5}Sr_{0.5}Al_2O_6$:Ce^{3+}, Mn^{2+}, *Inorg. Chem.*, 2017, **56**(1), 241–251.

18 K. Li, H. Lian, M. Shang and J. Lin, A novel greenish yellow-orange red $Ba_3Y_4O_9$:Bi^{3+}, Eu^{3+} phosphor with efficient energy transfer for UV-LEDs, *Dalton Trans.*, 2015, **44**(47), 20542–20550.

19 W. Lv, M. Jiao, Q. Zhao, B. Shao, W. Lü and H. You, $Ba_{1.3}Ca_{0.7}SiO_4$:Eu^{2+}, Mn^{2+}: a promising single-phase, color-tunable phosphor for near-ultraviolet white-light-emitting diodes, *Inorg. Chem.*, 2014, **53**(20), 11007–11014.

20 M. Ding, M. Xu and D. Chen, A new non-contact self-calibrated optical thermometer based on Ce^{3+} → Tb^{3+} → Eu^{3+} energy transfer process, *J. Alloys Compd.*, 2017, **713**, 236–247.

21 L. L. Wang, Q. L. Wang, X. Y. Xu, J. Z. Li, L. B. Gao, W. K. Kang, J. S. Shi and J. Wang, Energy transfer from Bi^{3+} to Eu^{3+} triggers exceptional long-wavelength excitation band in $ZnWO_4$:Bi^{3+}, Eu^{3+} phosphors, *J. Mater. Chem. C*, 2013, **1**(48), 8033–8040.

22 G. P. R. L. Blasse, Energy transfer in oxidic phosphors, *Phys. Lett. A*, 1968, **28**(6), 444–445.

23 H. Zhou, Q. Wang and Y. Jin, Temperature dependence of energy transfer in tunable white light-emitting phosphor $BaY_2Si_3O_{10}$:Bi^{3+}, Eu^{3+} for near UV LEDs, *J. Mater. Chem. C*, 2015, **3**(42), 11151–11162.

24 D. L. Dexter, A theory of sensitized luminescence in solids, *J. Chem. Phys.*, 1953, **21**(5), 836–850.

25 J. Cui, P. Li, L. Cao, X. Wang, Y. Yao, M. Zhang, M. Zheng, Z. Yang, H. Suo and Z. Wang, Achievement of broadband near-infrared phosphor $Ca_3Y_2Ge_3O_{12}$:Cr^{3+}, Ce^{3+} *via* energy transfer for food analysis, *J. Lumin.*, 2021, **237**, 118170–118176.